



## Efficient Photocatalytic Degradation of Methyl Orange and Methylene Blue under Visible Light Irradiation and Sunlight by TiO<sub>2</sub> Nanoparticles Using Novel Tridentate N<sub>2</sub>O Schiff Base Complexes

Ali Hossein Kianfar<sup>a,\*</sup>, Parisa Montazeri Najafabadi<sup>a</sup>, Maryam Sedighipoor<sup>a</sup>, Mohammad Mohsen Momeni<sup>a</sup>, Helmar Görls<sup>b</sup>, Winfried Plass<sup>b</sup> and Gholamhossein Mohammadnezhad<sup>a</sup>

<sup>a</sup>Department of Chemistry, Isfahan University of Technology, Isfahan, Iran, 84156-83111

<sup>b</sup>Institute of Inorganic and Analytical Chemistry, Chair of Inorganic Chemistry II, Friedrich Schiller University Jena, Humboldtstr. 8, 07743 Jena, Germany

(Received 11 October 2020, Accepted 8 January 2021)

Two novel heterocyclic Schiff base complexes ([VOL<sup>1</sup>(DMF)] [H<sub>2</sub>L<sup>1</sup> = (E)-1-((2-amino-5-nitrophenyl)imino-methyl) naphthalen-2-ol] and [VO<sub>2</sub>L<sup>2</sup>] [H<sub>2</sub>L<sup>2</sup> = (E)-1-((2-aminoethyl) imino-methyl)naphthalen-2-ol]) were synthesized and FT-IR, elemental analysis and UV-Vis spectroscopy were used to fully characterize them. Single-crystal X-ray diffraction was used to determine the structure of the [VO<sub>2</sub>L<sup>2</sup>] complex, in which the coordination around the vanadium ion is best described as distorted square pyramidal. The basal plane is formed by the donor atoms (NNO) of the Schiff base ligand and one of the oxo groups while the apical position is occupied by the other oxo group in the structure. The Schiff base complexes were loaded over TiO<sub>2</sub> photocatalyst and calcined at 450 °C. The MO<sub>x</sub>/TiO<sub>2</sub> structure and morphology were characterized by FT-IR, scanning electron microscopy (SEM), X-ray diffraction (XRD), EDX and solid state UV-Vis absorption. Photocatalytic oxidation of methyl orange (MO) and methylene blue (MB) dyes in aqueous media by solar and visible lights was used to evaluate the photocatalytic efficiency of MO<sub>x</sub>/TiO<sub>2</sub> semi-conducting nanoparticles. The incorporation of these complexes enhanced TiO<sub>2</sub> activation with visible light compared with naked TiO<sub>2</sub>, according to the results.

**Keywords:** Schiff base, X-ray diffraction, Photocatalytic efficiency, Methylene blue, Methyl orange

### INTRODUCTION

Considering the biological attributes and catalytic activity in different chemical and photochemical reactions, the chemistry of Schiff base complexes has been extensively studied [1-6]. Azo dyes, which constitute the largest class of dyes used in the industry are resistant to aerobic degradation. Biotreatment processes are based on natural soil microorganisms, which degrade dye compounds. This process is probably not sufficient given the resistance of the synthetic dyes to aerobic biodegradation. Therefore, the development of treatment technologies, which are more efficient, in the removal of

dyes from the waste streams, is necessary [7-10]. In the past few years, efforts have been devoted to the study of photochemical processes using semi-conducting oxides such as TiO<sub>2</sub>, CdS or ZnO in heterogeneous systems [11,12]. Titanium dioxide (TiO<sub>2</sub>) is one of the semiconductor catalysts, which has attracted much attention in photocatalysis. TiO<sub>2</sub>, which is the most efficient photocatalyst under the photon energy, maintains its stability after several catalytic runs while CdS and GaP are degraded to toxic compounds [13]. Nevertheless, the wide band gap of TiO<sub>2</sub> (3.2 eV) limits its broad application as a photocatalyst. Ultraviolet irradiation ( $\lambda < 387$  nm) is required for the photocatalytic activity of TiO<sub>2</sub>. Less than 5% of the solar radiation, which reaches the earth surface, can be used by TiO<sub>2</sub> [14]. In addition, the photo-quantum

\*Corresponding author. E-mail: [akianfar@iut.ac.ir](mailto:akianfar@iut.ac.ir)

yield value of TiO<sub>2</sub> is very small because of the photoinduced easy recombination of electron-hole pairs. Consequently, many efforts have been made to enhance the quantum efficiency of TiO<sub>2</sub> photocatalysts *via* doping by metal ions and clusters [15-17]. Metal ion doping is usually assumed to cause defects in the lattice or enhance the crystallinity of the catalyst and improve the photocatalytic efficiency [18,19]. Vanadium has frequently been investigated in this respect [20,21] since vanadium doping can result in the increased lifetime of the carrier and extended TiO<sub>2</sub> absorption range [22,23]. The preparation and characterization of vanadium-doped TiO<sub>2</sub> have been reported in many publications. Vanadium doping has recently been shown to provide a potentially promising approach to enhance the properties of photocatalytic materials. V-doped TiO<sub>2</sub> photocatalysts, which are quite active visible light, have been synthesized by Dostani and Kianfar [24,25]. In the present work, two novel Schiff base complexes ([VOL<sup>1</sup> (DMF)] and [VO<sub>2</sub>L<sup>2</sup>]) derived from tridentate Schiff base ligands have been successfully prepared and completely characterized using various analytical techniques. The complexes prepared were supported on semi-conducting TiO<sub>2</sub> nanoparticles and calcined by heating at 450 °C to yield V-doped TiO<sub>2</sub>. This work is aimed at the investigation of the photocatalytic effect of TiO<sub>2</sub> impregnated metal complexes. The catalytic activity of V-doped TiO<sub>2</sub> was evaluated in the photocatalytic degradation of methyl orange and methylene blue aqueous solutions using visible light or solar radiation. The effects of different reaction parameters such as reaction time, catalyst amount and solution pH on the degradation of the dyes have been studied. The catalytic activity has been measured in the successful photodegradation of MO and MB in aqueous media using visible light and solar irradiation.

## EXPERIMENTAL

### General Methods and Materials

Solvents and starting materials were supplied by Alfa Aesar. or Sigma Aldrich Chemical Co. and used without further purification. A JASCO V-570 spectrophotometer was used to record UV-Vis spectra. An FT-IR JASCO 680 plus spectrophotometer (KBr pellets) was used to obtain

infrared spectra. A CHN-O-Heraeus elemental analyzer was used to determine the elemental compositions. The X-ray diffraction patterns were recorded using a PANalytical XPRO MRD PW 3040 instrument. A MIRA3 TESCAN instrument was used to obtain FT-SEM images to determine the morphology of the samples. A Nonius Kappa CCD diffractometer was used to carry out the X-ray single crystal structure analyses.

### Synthesis of Tridentate Schiff Base Ligand H<sub>2</sub>L<sup>1</sup>

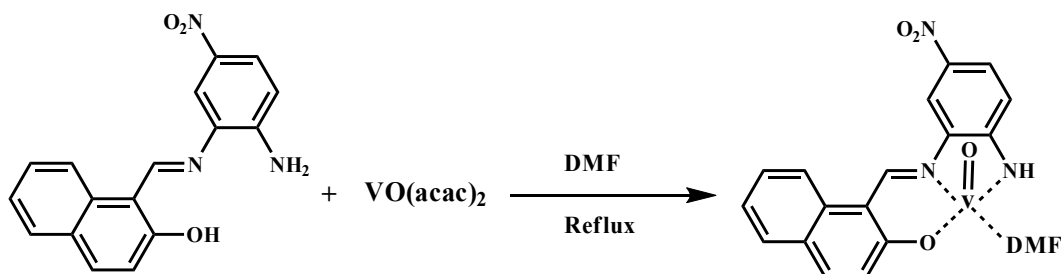
H<sub>2</sub>L<sup>1</sup> tridentate Schiff base ligand was prepared by the addition of 2-hydroxy-1-naphthaldehyde to a solution of 4-nitro-1,2-phenylenediamine in methanol (1:1 molar ratio), according to a reported method [26]. The resulting solution was then refluxed with stirring for 3 h. A light red precipitate formed during the reaction. Dichloromethane/methanol solvent mixture was used to recrystallize the products. H<sub>2</sub>L<sup>1</sup>, C<sub>17</sub>H<sub>13</sub>N<sub>3</sub>O<sub>3</sub>: FT-IR (KBr cm<sup>-1</sup>)  $\bar{\nu}_{\max}$ : 3346 and 3472 (NH<sub>2</sub>), 1628 (C=N), 1488 (C=C), 1316 (NO<sub>2</sub>), 1173 (C-O). UV-Vis,  $\lambda_{\max}$  (nm) ( $\epsilon$ , M<sup>-1</sup>cm<sup>-1</sup>) (DMF): 285 (81700), 349 (51800), 430 (11030). <sup>1</sup>H NMR (CDCl<sub>3</sub>,  $\delta$ , ppm) 4.80 (s, 2H, NH<sub>2</sub>), 6.80-8.40 (m, 9H, aromatic), 9.63 (s, 1H, HC=N), 14.43 (s, 1H, OH).

### Synthesis of Tridentate Schiff Base Ligand H<sub>2</sub>L<sup>2</sup>

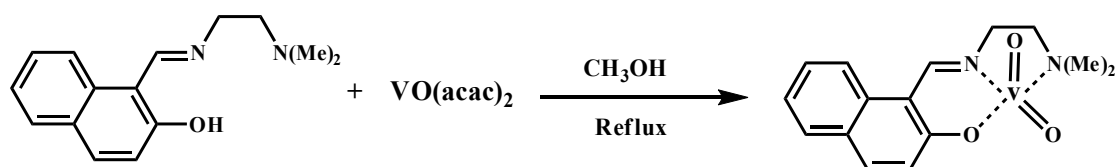
The tridentate H<sub>2</sub>L<sup>2</sup> Schiff base ligand was synthesized by condensation of 2-hydroxy-1-naphthaldehyde and N,N-dimethylethylenediamine (1:1 molar ratio) in 20 mL of methanol solvent. The solution obtained was heated at reflux for 3 h, followed by the addition of diethyl ether to obtain a yellow precipitate. FT-IR (KBr cm<sup>-1</sup>)  $\bar{\nu}_{\max}$ : 2800-3100 (C-H (CH<sub>2</sub> and CH<sub>3</sub>)), 1634 (C=N), 1518 (C=C), 1183 (C-O). UV-Vis,  $\lambda_{\max}$  (nm) ( $\epsilon$ , M<sup>-1</sup>cm<sup>-1</sup>) (Ethanol): 231 (158000), 310 (36000), 399 (35300), 422 (35600).

### Synthesis of Vanadyl Schiff Base Complex [VOL<sup>1</sup> (DMF)]

5 mL of a solution of H<sub>2</sub>L<sup>1</sup> Schiff base ligand (1 mmol) in DMF were added to 10 mL of a solution of VO (acac)<sub>2</sub> (1 mmol) in methanol. The reaction mixture was then heated at reflux while stirring for 4 h to yield a precipitate, which was then filtered, washed and re-crystallized from a mixture of methanol and dichloromethane solvents (Scheme 1). Anal., calcd. for C<sub>20</sub>H<sub>18</sub>N<sub>4</sub>O<sub>5</sub>V: C, 54.63; H,



Scheme 1. The structure of Schiff base ligand and its complex



Scheme 2. The structure of Schiff base ligand and its complex

3.76; N, 11.83%. Found; C, 53.94; H, 4.07; N, 12.50%. FT-IR (KBr  $\text{cm}^{-1}$ )  $\nu_{\text{max}}$ : 1627 (C=N), 1521 (C=C), 1337 ( $\text{NO}_2$ ), 1660 (C=O), 976 (V=O), 3432 (NH). UV-Vis,  $\lambda_{\text{max}}$  (nm) ( $\epsilon$ ,  $\text{M}^{-1} \text{cm}^{-1}$ ) (DMF): 276 (70300), 331(39000), 466 (5300).

### Synthesis of Vanadyl Schiff Base Complex $[\text{VO}_2\text{L}^2]$

10 mL of a methanolic solution of  $\text{H}_2\text{L}^2$  tridentate Schiff base ligand (1 mmol) were added to 10 mL of a solution of  $\text{VO}(\text{acac})_2$  (1 mmol) in methanol. The color of the solution thus obtained instantly converted to dark green. The reaction mixture was then refluxed while stirring for 1 h to form a green precipitate, which was filtered, washed with methanol and re-crystallized from a mixture of methanol and dichloromethane solvents. Anal., calcd. for  $\text{C}_{15}\text{H}_{17}\text{N}_2\text{O}_3\text{V}$ : C, 56.86; H, 5.90; N, 7.94%. Found; C, 55.65; H, 5.28; N, 8.64%, FT-IR (KBr  $\text{cm}^{-1}$ )  $\bar{\nu}_{\text{max}}$ : 2800-3100 (C-H ( $\text{CH}_2$  and  $\text{CH}_3$ )), 1633 (C=N), 1511 (C=C), 976 (V=O). UV-Vis,  $\lambda_{\text{max}}$  (nm) ( $\epsilon$ ,  $\text{M}^{-1} \text{cm}^{-1}$ ) (Ethanol): 234 (83500), 313 (32500), 407 (16700) (Scheme 2).

### Crystal Structure Specification of $[\text{VO}_2\text{L}^2]$

A Nonius Kappa CCD diffractometer was applied to obtain the intensity data using graphite-monochromated

$\text{Mo-K}_\alpha$  radiation. The data were reformed for polarization effects and Lorentz. The absorption was taken into consideration on a semi-empirical basis using multiple scans [27-29]. Direct procedures (SHELXS [30]) were used to solve the structure, followed by refining by full-matrix least squares techniques against  $\text{Fo}^2$  (SHELXL-97 [30]). All hydrogen atoms of  $\text{VO}_2\text{L}^2$  were located by difference Fourier synthesis and isotropically refined. All non-hydrogen atoms were anisotropically refined [30]. An XP instrument (SIEMENS Analytical X-ray Instruments, Inc. 1994; Madison, WI, USA.) was used for structure representations.

### Synthesis of $[\text{VOL}^1(\text{DMF})]/\text{TiO}_2$ and $[\text{VO}_2\text{L}^2]/\text{TiO}_2$

$[\text{VOL}^1(\text{DMF})]/\text{TiO}_2$  and  $[\text{VO}_2\text{L}^2]/\text{TiO}_2$  nanoparticles were prepared at ambient temperature by reacting a solution of  $[\text{VOL}^1(\text{DMF})]$  and  $[\text{VO}_2\text{L}^2]$  complexes (0.1 g) and 0.5 g of  $\text{TiO}_2$  nanoparticles suspended in DMF (in methanol for  $[\text{VO}_2\text{L}^2]$ ). The reaction mixture was stirred for 6 h to incorporate the complexes onto  $\text{TiO}_2$  NPs. The red and green precipitates obtained, respectively were washed several times with methanol. Finally, the solids were dried for 24 h at 40 °C.

### Synthesis of $\text{V}_2\text{O}_5/\text{TiO}_2$ Nano-metal Mixed Oxide

To synthesize nano-metal mixed oxide, V-doped  $\text{TiO}_2$ ,

the mixture of nanoparticles and vanadium metal complexes ( $[\text{VOL}^1(\text{DMF})]/\text{TiO}_2$  and  $[\text{VO}_2\text{L}^2]/\text{TiO}_2$ ) were calcined in an oven for 4 h at the temperatures of up to 450 °C. Following heating, the color of nanoparticles and complex mixture converted to pale yellow.

### Photocatalytic Experiments under Visible Light

The photocatalytic activities of all the prepared samples were assessed in the degradation of the aqueous methylene blue and methyl orange under visible light irradiation. The photocatalytic reactions were carried out in a single compartment cylindrical quartz reactor. A 200 W xenon lamp with a luminous intensity of 100 mW cm<sup>-2</sup> was applied as the light source. The experiments were performed at ambient temperature. The general photocatalytic procedure was as follows: 20 mg. of the catalyst were suspended in a fresh dye solution ( $C_0 = 2 \text{ mg L}^{-1}$ ) in water. The suspension was then stirred in the dark for 2 h to establish adsorption-desorption equilibrium of MB and MO dyes, followed by exposure to visible light irradiation under magnetic stirring for 2 h. Aliquots were taken at specific times and the photocatalysts were removed by centrifugation. Afterwards, UV-Vis spectroscopy was used to observe changes in the concentrations of MB and MO.

### Photocatalytic Experiments under Natural Sunlight

All solar photocatalytic tests were performed under identical sunny conditions, spring days. The experiments were carried out in sets simultaneously and the results were compared to overcome the problem of variations in sunlight intensity even in a clear sky. The experiments were performed using the appendix procedure: (1) Stock aqueous solutions of the dye were prepared by dissolving known quantities of the dye in distilled water. (2) A known amount of the photocatalyst was added to a known volume of the aqueous dye solution at a certain pH and the resulting mixture was stirred. (3) The dye solution was irradiated by sunlight focused on the photoreaction structure. Aliquots were taken at specific times and the photocatalysts were removed by centrifugation. Afterwards, UV-Vis spectroscopy was used to observe changes in the concentrations of MB and MO. The experiments were carried out several times to investigate the effects of various parameters such as initial dye concentration, irradiation

intensity, catalyst amount and pH of solution.

## RESULTS AND DISCUSSION

### Determination of the Molecular Structure of the Vanadyl Schiff Base Complex

The vanadyl complex and its structure with the atom numbering design are shown in Fig. 1. As observed, the donor atoms of tridentate Schiff base ligand and one oxido ligand (O1) form the equatorial plane and the other oxo ligand is placed at the apex. The unequal distances and angles of metal-ligand bond indicate the distorted square pyramidal geometry of vanadium(IV) ion: *i.e.* V-N1 = 2.1244(15), V-N2 = 2.1713(15), V-O1 = 1.9085(13), V-O2 = 1.6195(13), V-O3 = 1.6346(13) Å and O3-V-O1, O3-V-O2, O1-V-O2, O3-V-N2, O1-V-N2, O2-V-N2, O3-V-N1, O1-V-N1, O2-V-N1, N2-V-N1 angles are appropriated in the range of 97.77(6)°, 110.52(8)°, 104.70(6)°, 88.21(6)°, 153.67(6)°, 97.01(6)°, 141.41(7)°, 82.59(6)°, 106.57(7)° and 77.00(6)°, respectively. All distances and angles in the vanadyl complex match those of other vanadium(IV) complexes [31]. The experimental details and crystal data are shown in Tables 1 and 2. The structure of the complex is characterized using X-ray diffraction and crystallization in the monoclinic, space group  $P2_1/c$ .

### FT-IR Characterization

The important changes of the main bands were investigated by analyzing the FT-IR spectra of the synthesized complexes and the Schiff bases. The peaks corresponding to the C=N bond of azomethine group are observed at 1628 and 1634 cm<sup>-1</sup> in the spectra of the H<sub>2</sub>L<sup>1</sup> and H<sub>2</sub>L<sup>2</sup> free Schiff bases, respectively. These are shifted to the lower frequencies in the spectra of the  $[\text{VOL}^1(\text{DMF})]$  and  $[\text{VO}_2\text{L}^2]$  complexes in the 1627-1633 cm<sup>-1</sup> range, indicating that the lone electron pair of the C=N nitrogen atom is coordinated to the vanadyl ions [32]. The NH<sub>2</sub> stretching frequencies are observed at 3346 and 3472 cm<sup>-1</sup> in the FT-IR spectrum of H<sub>2</sub>L<sup>1</sup> ligand whereas the symmetrical vibrational frequency of NO<sub>2</sub> is observed at 1316 cm<sup>-1</sup>. The N-H vibration appears as a single peak at about 3432 cm<sup>-1</sup> in the FT-IR spectrum of  $[\text{VOL}^1(\text{DMF})]$  complex, indicating the change of NH<sub>2</sub> functional group to

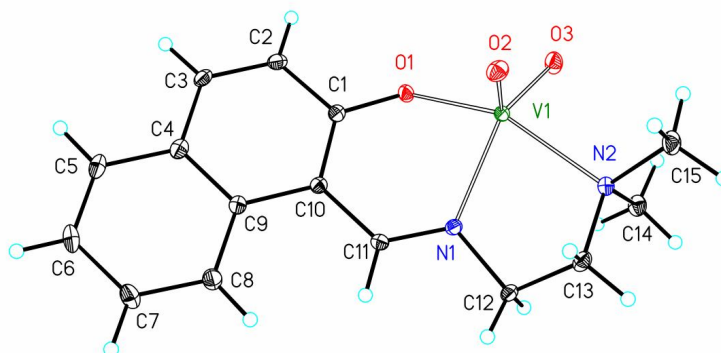


**Fig. 1.** Structure of  $\text{VO}_2\text{L}^2$  complex.

**Table 1.** Selected Bond Distances (Å) and Bond Angles (°) for [VO (L)] Complex

Bond distances		Bond angles	
V1-N1	2.1244(15)	O(2)-V(1)-O(3)	110.52(8)
V1-N2	2.1713(15)	O(2)-V(1)-O(1)	104.70(6)
V1-O1	1.9085(13)	O(3)-V(1)-O(1)	97.77(6)
V1-O2	1.6195(13)	O(2)-V(1)-N(1)	106.57(7)
V1-O3	1.6346(13)	O(3)-V(1)-N(1)	141.41(7)
O1-C1	1.318(2)	O(1)-V(1)-N(1)	82.59(6)
N1-C11	1.293(2)	O(2)-V(1)-N(2)	97.01(6)
N1-C12	1.471(2)	O(3)-V(1)-N(2)	88.21(6)
N2-C15	1.471(2)	O(1)-V(1)-N(2)	153.67(6)
N2-C14	1.486(2)	N(1)-V(1)-N(2)	77.00(6)
N2-C13	1.491(2)		

NH following the coordination of Schiff base ligand. The  $\text{NO}_2$  stretching frequency of  $[\text{VOL}^1 (\text{DMF})]$  complex is observed at  $1337 \text{ cm}^{-1}$ . Moreover, in the IR spectrum of  $[\text{VOL}^1 (\text{DMF})]$  complex, a new peak appearing at  $1660 \text{ cm}^{-1}$  corresponds to the  $\text{C}=\text{O}$  of the coordinated DMF. The C-H vibration frequencies in the range of  $2800\text{--}3100 \text{ cm}^{-1}$  are due to the aliphatic C-H vibration of  $\text{H}_2\text{L}^2$  and  $[\text{VO}_2\text{L}^2]$  complex. The IR spectra of the ( $[\text{VOL}^1 (\text{DMF})]$ ) and  $[\text{VO}_2\text{L}^2]$  complexes exhibit a band at  $976 \text{ cm}^{-1}$ , which

could be ascribed to the stretching frequency of  $(\text{V}=\text{O})$  [33]. The presence of this particular band in this region confirms the formation of vanadyl Schiff base complexes. The IR spectrum of pure  $\text{TiO}_2$  nanoparticles, complex and the complex formed on the surface of  $\text{TiO}_2$  NPs before and after calcination are shown in Figs. 2 and 3. The FT-IR spectra of pure  $\text{TiO}_2$  and V- $\text{TiO}_2$  show absorption peaks at  $3421$  and  $1635 \text{ cm}^{-1}$ , respectively. The absorption peak at  $3421 \text{ cm}^{-1}$  corresponds to O-H stretching modes originating from the

**Table 2.** Crystallographic and Structure Refinement Data for VOL Complex

Compound	(A)
Formula	C <sub>15</sub> H <sub>17</sub> N <sub>2</sub> O <sub>3</sub> V
Formula weight (g mol <sup>-1</sup> )	324.25
Temperature (K)	133
Wavelength $\lambda$ (Å)	0.71073
Crystal system	Monoclinic
Space group	<i>P2<sub>1</sub>/c</i>
Crystal size (mm <sup>3</sup> )	0.132 × 0.104 × 0.088
<i>a</i> (Å)	13.3926(3)
<i>b</i> (Å)	9.7719(2)
<i>c</i> (Å)	12.1758(3)
$\alpha$ (°)	90
$\beta$ (°)	114.746(1)
$\gamma$ (°)	90
Volume (Å <sup>3</sup> )	1447.14(6)
<i>Z</i>	4
Density (calcd.) (g cm <sup>-3</sup> )	1.488
$\theta$ Ranges for data collection	2.67°-27.47°
<i>F</i> (000)	672
Absorption coefficient (mm <sup>-1</sup> )	0.696
Index ranges	-17 ≤ <i>h</i> ≤ 17 -10 ≤ <i>k</i> ≤ 12 -15 ≤ <i>l</i> ≤ 11
Reflections collected	8352
Independent reflections	3280
<i>R</i> <sub>int</sub>	0.0363
Completeness $\theta$ max	99.2%
Max. and min. transmission	0.7456 and 0.6570
Parameters, restraints	258, 0
Final <i>R</i> <sub>1</sub> , <i>wR</i> <sub>2</sub> <sup>a</sup> (Obs. data)	0.0351, 0.0833
Final <i>R</i> <sub>1</sub> , <i>wR</i> <sub>2</sub> <sup>a</sup> (All data)	0.0407, 0.0869
Goodness of fit on <i>F</i> <sup>2</sup> (S)	1.077
Largest diff peak and hole (e Å <sup>-3</sup> )	0.336 and -0.342

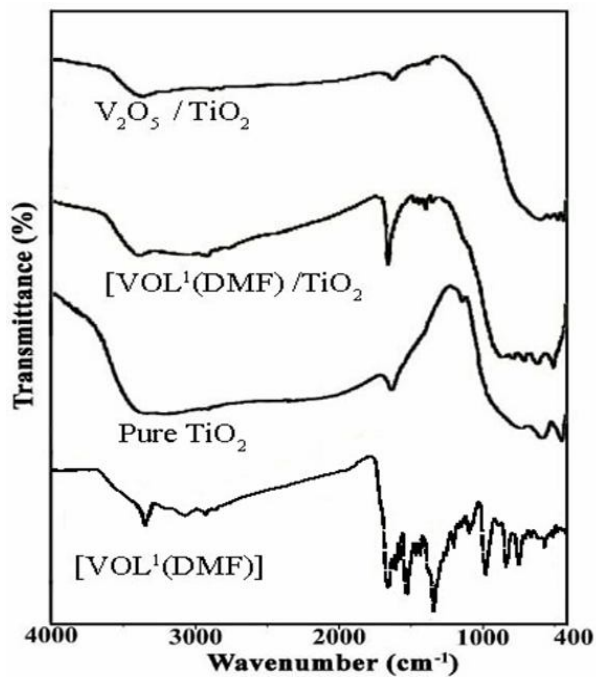


**Fig. 2.** The FT-IR spectra of pure  $TiO_2$  NPs,  $[VOL^1(DMF)]$  complex,  $([VOL^1(DMF)])/TiO_2$  and  $V_2O_5/TiO_2$ .

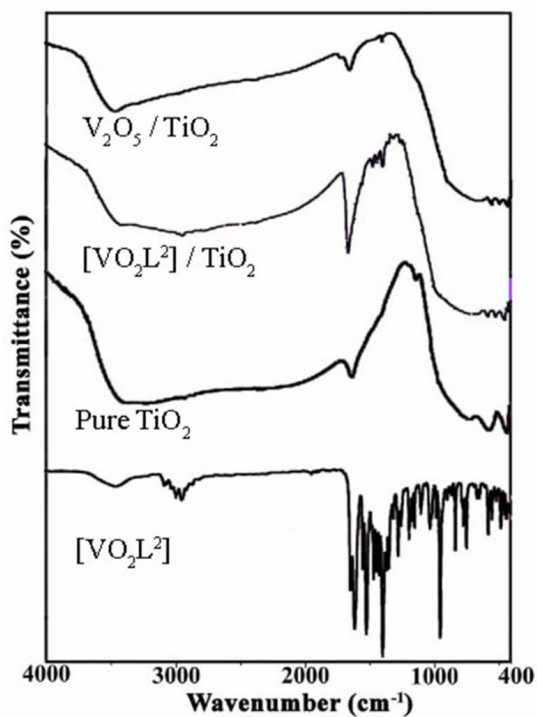


**Fig. 3.** The FT-IR spectra of pure  $TiO_2$  NPs,  $[VO_2L^2]$  complex,  $[VO_2L^2]/TiO_2$  and  $V_2O_5/TiO_2$ .

surface water molecule, which is due to the physical absorption of water [34,35]. The -OH bending modes originating from the surface of TiO<sub>2</sub> appear at 1635 cm<sup>-1</sup>. There are characteristic wide peaks in the 1000-500 cm<sup>-1</sup> range, which are ascribed to the bending vibration of the Ti-O bonds [36]. The IR spectra of the ([VOL<sup>1</sup> (DMF)]) and [VO<sub>2</sub>L<sup>2</sup>] complexes, which support the surface of TiO<sub>2</sub> nanoparticles, can confirm the presence of the complexes on the surface of NPs and the interaction between them. The peaks observed at 1628 and 1634 cm<sup>-1</sup> correspond to the imine functional group of the complex. The IR spectrum of V-doped TiO<sub>2</sub> has also been recorded after calcination of the complexes at 450 °C. The absorption spectra of TiO<sub>2</sub> bands previously indicated are well visible.

### Electronic Spectra

The UV-Vis spectral data of the ligands and complexes are shown in the experimental sections. All the bands below 400 nm in the UV-Vis spectra correspond to the  $\pi \rightarrow \pi^*$  transition of the aromatic ring. In the meantime, all the bands above 400 nm are due to the  $\pi \rightarrow \pi^*$  and  $n \rightarrow \pi^*$  excitations, which are associated with the azomethine group [32,37,38]. Figures 4 and 5 show the solid state UV-Vis absorption spectra of TiO<sub>2</sub> nanoparticles and the modified semiconductors with ([VOL<sup>1</sup> (DMF)]) and [VO<sub>2</sub>L<sup>2</sup>] complexes. The shift to the longer wavelength and transformation in the absorption spectrum of the nanocomposite, in comparison with TiO<sub>2</sub>, is likely to correspond to the synthesis of the nano metal mixed oxide [24].

### X-ray Diffraction

The XRD analysis in the range of  $2\theta = 5^\circ$ - $80^\circ$  shows crystalline structure of pure TiO<sub>2</sub> and a successful interaction between the complexes and TiO<sub>2</sub> nanoparticles before and after calcination at the temperature of 450 °C. Figures 6 and 7 show the XRD spectra of pure TiO<sub>2</sub> nanoparticles, [VOL<sup>1</sup> (DMF)]/TiO<sub>2</sub>, [VO<sub>2</sub>L<sup>2</sup>]/TiO<sub>2</sub> and V-doped TiO<sub>2</sub> nanoparticles. Matching the characteristic peaks in the XRD pattern of TiO<sub>2</sub> nanoparticles at 70(220), 62(204), 55(211), 53(105), 48(200), 38(112), 36(004), 35(103) and 25(101) confirmed the anatase phase [39]. Rutile and anatase phases are observed in the XRD pattern of V<sub>2</sub>O<sub>5</sub>/TiO<sub>2</sub>. The electrons of TiO<sub>2</sub> nanoparticles at the

conduction band of anatase were transmitted to that of the rutile phase by forming the mixed rutile-anatase phases. This improves the photocatalytic activity of the TiO<sub>2</sub> nanoparticles. Several new characteristic peaks corresponding to the metal oxide and the rutile phase are observed in the XRD pattern of V<sub>2</sub>O<sub>5</sub>/TiO<sub>2</sub> in comparison with the XRD pattern of pure TiO<sub>2</sub> nanoparticles [40,41].

### Morphology Analysis

The scanning electron microscopy (SEM) images and the corresponding size distribution histograms of calcined [VOL<sup>1</sup> (DMF)]/TiO<sub>2</sub> and [VO<sub>2</sub>L<sup>2</sup>]/TiO<sub>2</sub> are shown in Figs. 8 and 9. As observed, the particles are almost spherical with sizes in the nanometer range. A Gaussian profile with a narrow size distribution is shown by the size distribution. The average diameters, which were calculated using the Gaussian fitting of histogram, are 18.83 and 47.21 nm for [VOL<sup>1</sup> (DMF)]/TiO<sub>2</sub> and calcined [VO<sub>2</sub>L<sup>2</sup>]/TiO<sub>2</sub>, respectively. The obtained nanospheres are homogenous considering the standard deviation value.

### SEM/EDX Analysis

SEM/EDX was used to analyze the compositions of [VOL<sup>1</sup> (DMF)]/TiO<sub>2</sub> and [VO<sub>2</sub>L<sup>2</sup>]/TiO<sub>2</sub> after calcination. The presence of Ti, V and O elements after annealing is clearly observed in Figs. 10 and 11.

### Photocatalytic Studies under Visible Light Irradiation

The degradation of methylene blue and methyl orange in aqueous media by visible light was used to monitor the photocatalytic activity of the new nanocomposites. The UV-Vis spectra of nanocomposites were recorded at different time intervals to determine the photocatalytic activities of bare and modified TiO<sub>2</sub> samples. In addition, the variations in the intensity at  $\lambda_{\max}$  of MB and MO were used to detect the rate of methylene blue and methyl orange decomposition. The photodegradation yield is defined as:

$$\text{Photodegradation yield (\%)} = [(C_0 - C)/C_0] \times 100 \quad (1)$$

where  $C_0$  and  $C$  are the concentrations of the initial and photodegraded dyes under visible light irradiation at different time intervals, respectively. The photocatalytic

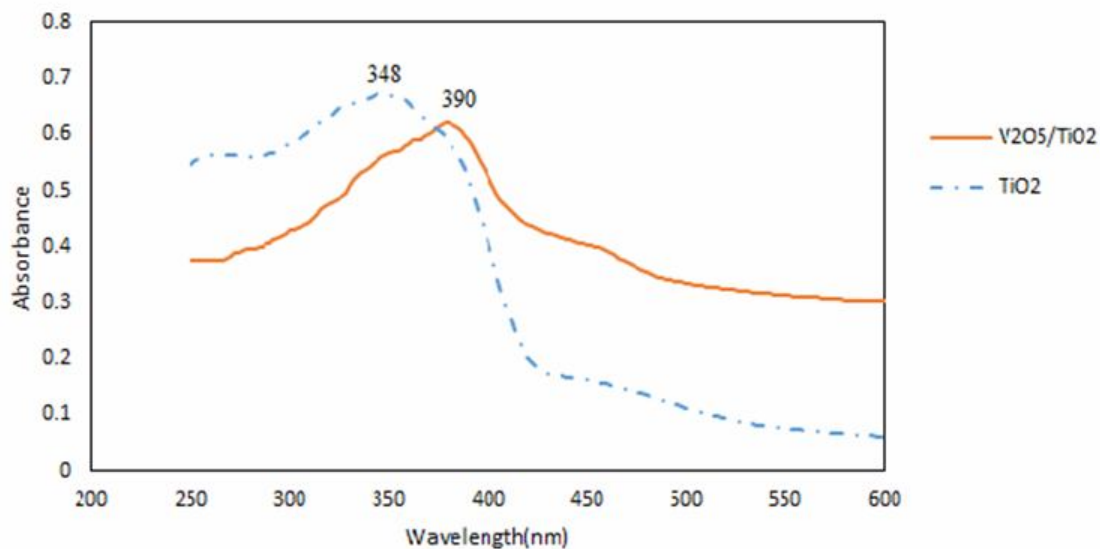


**Fig. 4.** The solid UV-Vis spectra of TiO<sub>2</sub> and V<sub>2</sub>O<sub>5</sub>/TiO<sub>2</sub>.

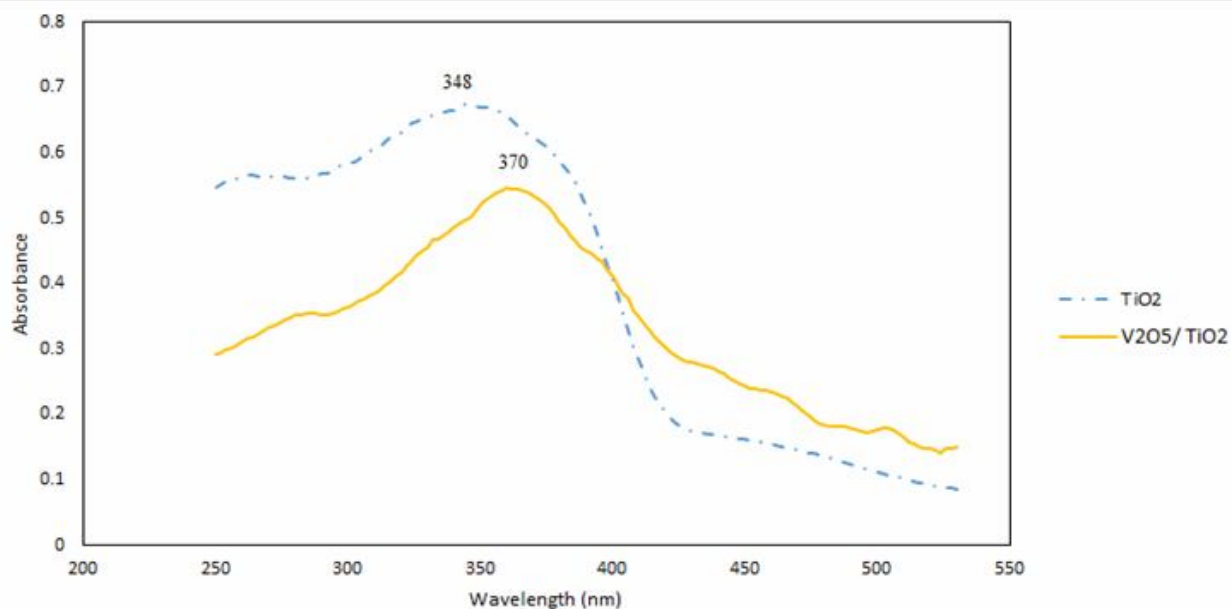


**Fig. 5.** The solid UV-Vis of spectra TiO<sub>2</sub> and V<sub>2</sub>O<sub>5</sub>/TiO<sub>2</sub>.

process was very efficient in methylene blue removal; according to the photocatalysis results. The photodegradation rates of MB and MO under xenon

lamp irradiation in the presence of TiO<sub>2</sub> nanoparticles, calcined [VOL<sup>1</sup> (DMF)]/TiO<sub>2</sub> (S1) and calcined [VO<sub>2</sub>L<sup>2</sup>]/TiO<sub>2</sub> (S2) are shown in Fig. 12. As observed, the

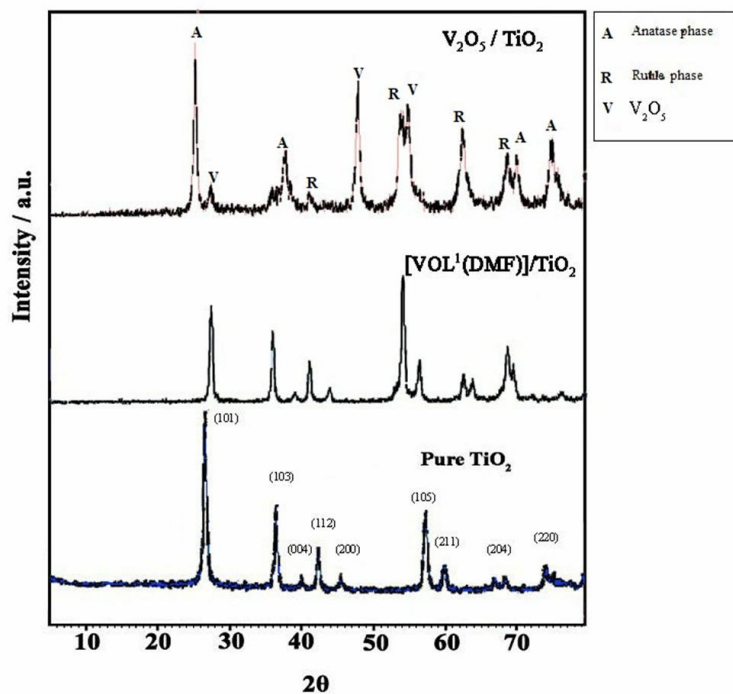


Fig. 6. The XRD patterns of pure  $TiO_2$  NPs,  $[VOL^1(DMF)]/TiO_2$  and  $V_2O_5/TiO_2$ .

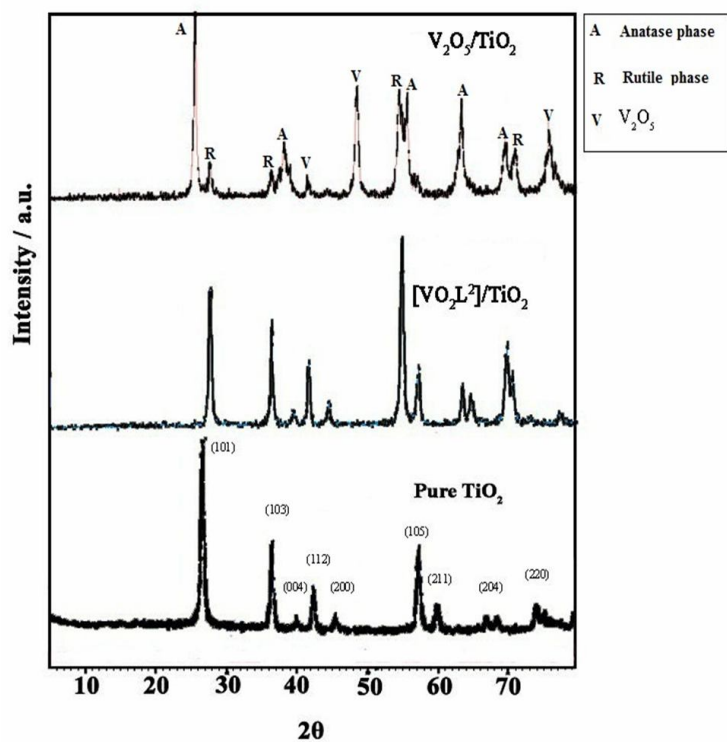
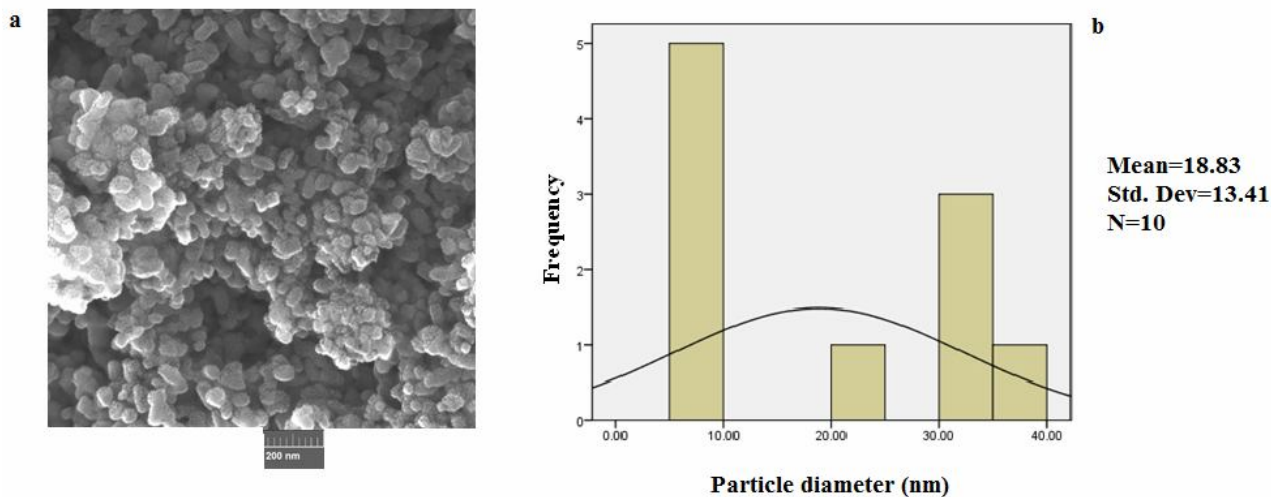
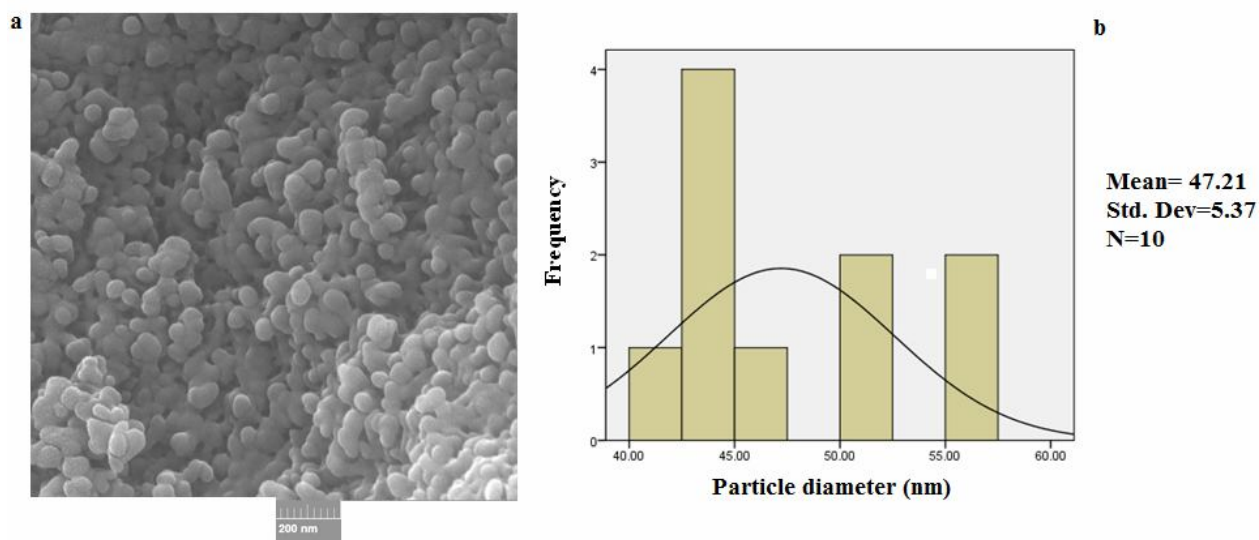


Fig. 7. The XRD patterns of pure  $TiO_2$  NPs,  $[VO_2L^2]/TiO_2$  and  $V_2O_5/TiO_2$ .



**Fig. 8.** (a) SEM image and (b) particle size distribution histograms of calcined [VOL<sup>1</sup>(DMF)]/TiO<sub>2</sub>.



**Fig. 9.** (a) SEM image and (b) particle size distribution histograms of calcined [VO<sub>2</sub>L<sup>2</sup>]/TiO<sub>2</sub>.

photocatalytic degradation efficiencies of MB and MO for a 360 min period over calcined [VOL<sup>1</sup>(DMF)]/TiO<sub>2</sub> was 90%, yielding the maximum removal rate. Photocatalytic reaction kinetics can be expressed by the Langmuir-Hinshelwood (L-H) model [42-45]:

$$\ln(C_0/C) = k_{app} t \quad (2)$$

where  $k_{app}$  is the apparent pseudo-first order reaction rate constant and  $t$  is the reaction time. A plot of  $\ln(C_0/C)$  vs.  $t$  will yield a slope of  $k_{app}$ . Tables 3 and 4 show the calculated  $k_{app}$  and correlation coefficients corresponding to Fig. 13. The photocatalyst stability is also significant for practical applications since it can be regenerated and recycled. The recyclability of calcined V-doped TiO<sub>2</sub> samples was studied

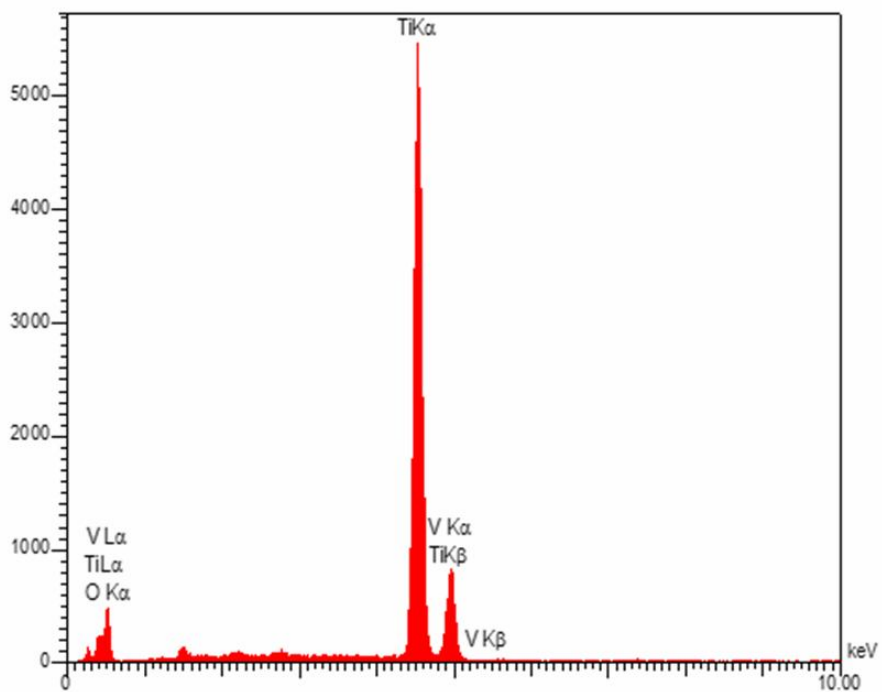


**Fig. 10.** EDX spectra of calcined [VOL<sup>1</sup>(DMF)]/TiO<sub>2</sub>.

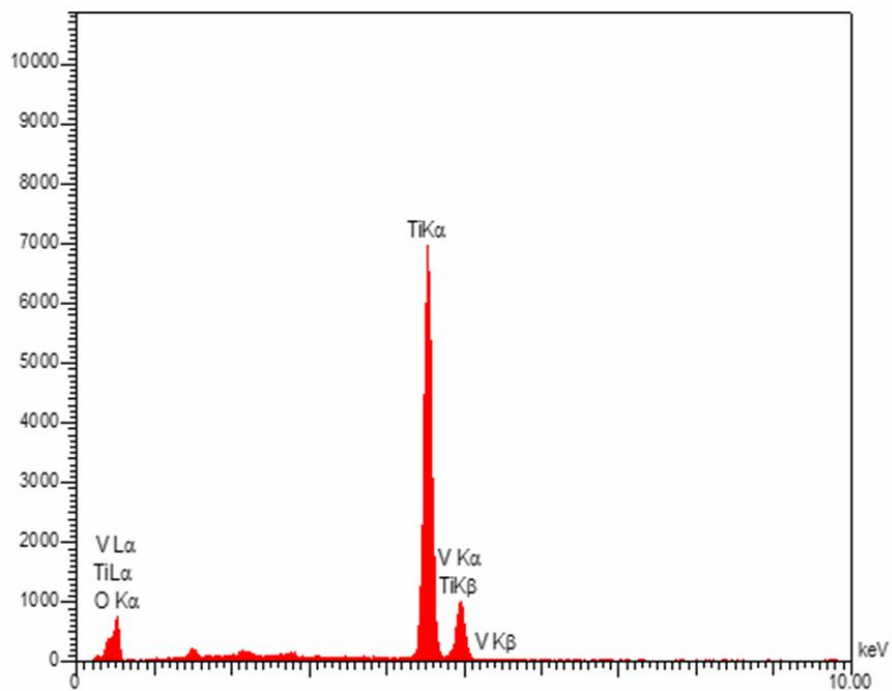


**Fig. 11.** EDX spectra of calcined [VO<sub>2</sub>L<sup>2</sup>]/TiO<sub>2</sub>.

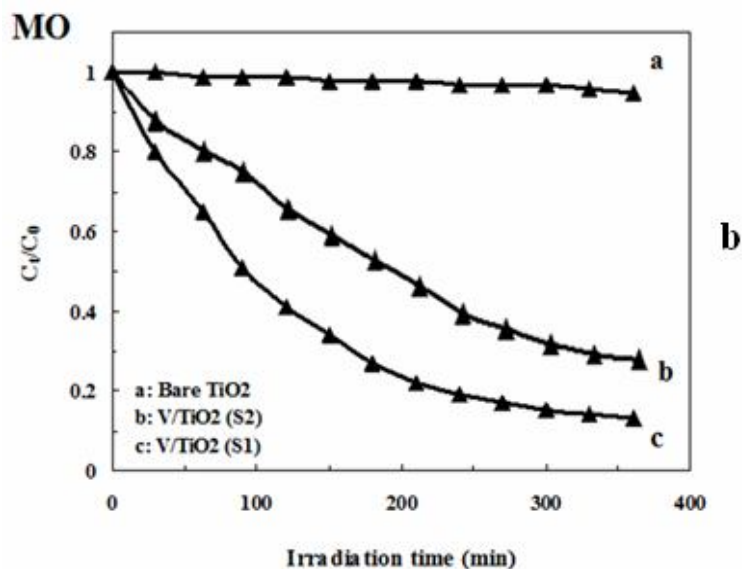


**Fig. 12.** (a) The photocatalytic degradation of MB and (b). The photocatalytic degradation of MO over the different samples under xenon light irradiation.

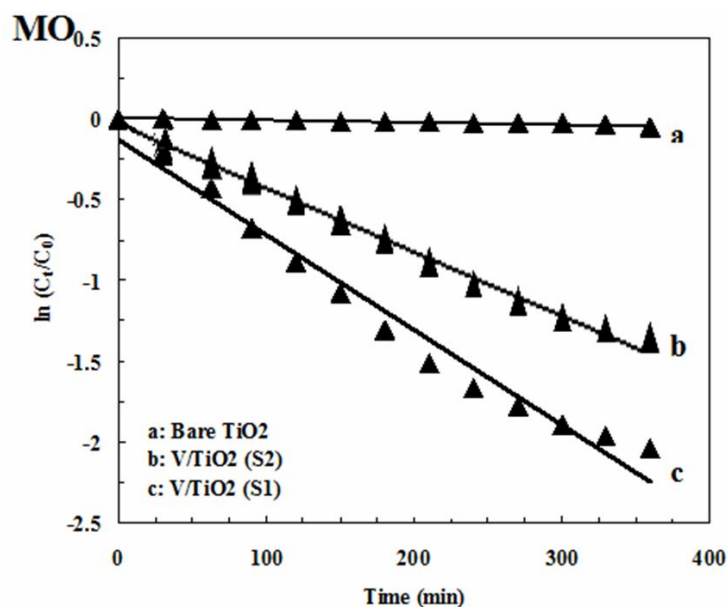


**Fig. 13.**  $\ln(C_t/C_0)$  vs. irradiation time plot.

via monitoring the catalytic activity during successive runs. As observed in Fig. 14, similar catalytic performance was shown by the catalyst with no significant deactivation after

four runs, which indicates its high stability after multiple uses.

Sample S1 showed the highest rate constants for MB

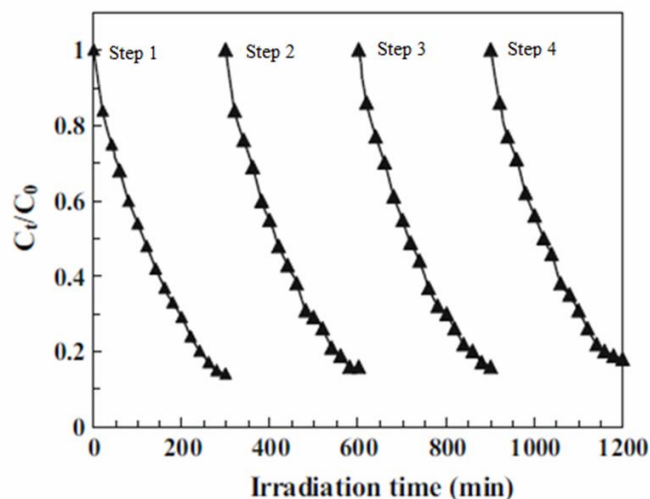


**Fig. 14.** Photocatalyst stability test of doped TiO<sub>2</sub>-calcined.

**Table 3.** The Apparent First-order Rate Constant ( $k$ ) of Photocatalytic Degradation of MB for Different Samples

Samples	Apparent rate constant ( $k$ (min <sup>-1</sup> ))	Correlation coefficient ( $R^2$ )
Undoped TiO <sub>2</sub>	$1.30 \times 10^{-2}$	0.9983
[VOL <sup>1</sup> (DMF)]/TiO <sub>2</sub> calcined form (S1)	$2.3 \times 10^{-2}$	0.9896
[VO <sub>2</sub> L <sup>2</sup> ]/TiO <sub>2</sub> calcined form (S2)	$5.4 \times 10^{-2}$	0.9936

**Table 4.** The Apparent First-order Rate Constant ( $k$ ) of Photocatalytic Degradation of MO for Different Samples

Samples	Apparent rate constant ( $k$ (min <sup>-1</sup> ))	Correlation coefficient ( $R^2$ )
Undoped TiO <sub>2</sub>	$1.30 \times 10^{-2}$	0.9983
[VOL <sup>1</sup> (DMF)]/TiO <sub>2</sub> calcined form (S1)	$2.3 \times 10^{-2}$	0.9896
[VO <sub>2</sub> L <sup>2</sup> ]/TiO <sub>2</sub> calcined form (S2)	$5.4 \times 10^{-2}$	0.9936

and MO degradation and effectively enhanced the photocatalytic activity in MB and MO degradation. The lowest photocatalytic activity was that of pure TiO<sub>2</sub> since this sample could only absorb UV light. The higher

photocatalytic activity of the doped samples may be due to the combined effect of several factors such as the doped material type and increased light-harvesting ability (the capability of absorption of visible and higher lights

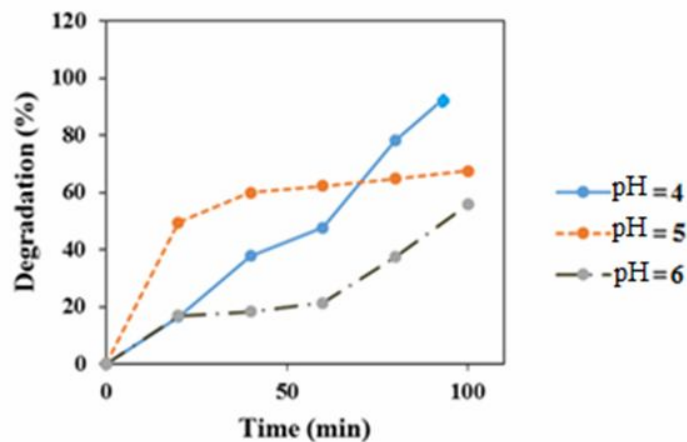


**Fig. 15.** Effect of pH on MO removal over calcined [VOL<sup>1</sup> (DMF)]/TiO<sub>2</sub> under sunlight (catalyst loading = 10 mg L<sup>-1</sup>, irradiation time = 100 min, initial MO dye concentration = 5 ppm).

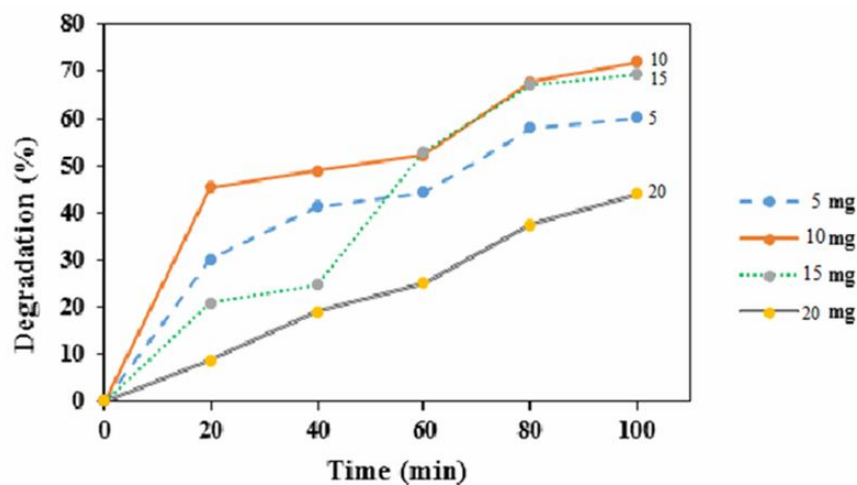


**Fig. 16.** Effect of catalyst loading on removal of MO over calcined [VOL<sup>1</sup> (DMF)]/TiO<sub>2</sub> under sunlight (pH = 4, irradiation time = 100 min, initial MO dye concentration = 5 ppm).

compared to pure TiO<sub>2</sub>) [25].

### Photocatalytic Performance under Sunlight and Different Conditions

**Effect of pH.** The surface charge property of the photocatalyst, molecule charge, molecule adsorption onto the photocatalyst surface and hydroxyl radical concentration affect the photocatalytic degradation efficiency. Since these properties are pH dependent, they play significant parts in

the degradation of pollutants. Figure 15 shows the effect of pH on the photocatalytic degradation of MO dye over calcined [VOL<sup>1</sup> (DMF)]/TiO<sub>2</sub> under sunlight. The solution pH is adjusted prior to irradiation and not controlled during the reaction. According to the experimental results, the photocatalytic degradation efficiency of calcined [VOL<sup>1</sup> (DMF)]/TiO<sub>2</sub> under sunlight is higher at pH = 4. Therefore, the strong adsorption of MO on the catalyst surface is responsible for the higher degradation efficiency.

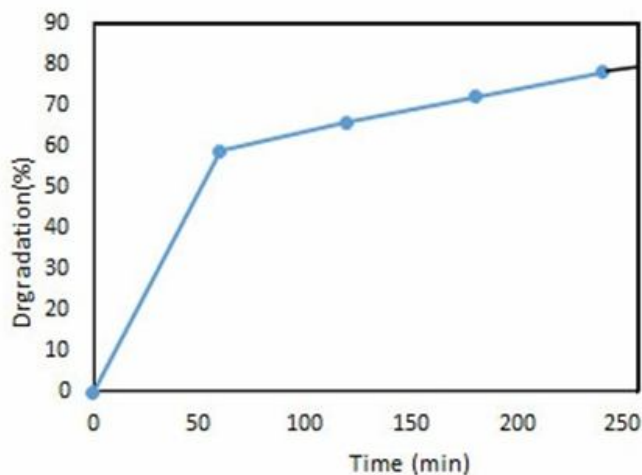


**Fig. 17.** Effect of time on removal of MO over calcined [VOL<sup>1</sup>(DMF)]/TiO<sub>2</sub> under sunlight (catalyst loading = 10 mg L<sup>-1</sup>, pH = 4, initial MO dye concentration = 5 ppm).

The reaction solution pH strongly affects the TiO<sub>2</sub> photocatalytic activity because of its amphoteric nature. The TiO<sub>2</sub> surface charge changes with pH. The point of zero charge (pzc) for TiO<sub>2</sub> is at pH ≈ 6.5. The TiO<sub>2</sub> surface is positively charged in acid solutions (pH < pzc), but negatively charged in basic media (pH > pzc) [46]. At lower pH values, more protons are produced, which may be absorbed on the TiO<sub>2</sub> surface, making the particles positively charged. Positively charged TiO<sub>2</sub> particles help the migration of photoinduced electrons, which may react with adsorbed O<sub>2</sub> to form O<sub>2</sub><sup>•-</sup> (e<sup>-</sup> + O<sub>2</sub> → O<sub>2</sub><sup>•-</sup>). Moreover, the recombination of electrons and holes can also be inhibited by positively charged TiO<sub>2</sub> particles. This generates more OH<sup>•</sup> *via* the reaction of holes and water. Both O<sub>2</sub><sup>•-</sup> and OH<sup>•</sup> radical ions are strong oxidants [47,48], which could account for the improved degradation of MO. Likewise, negative charges in alkaline media favor the migration of the hole to TiO<sub>2</sub> surface and OH<sup>•</sup> generation [49,50]. In neutral pH, TiO<sub>2</sub> surface is not charged and neither O<sub>2</sub><sup>•-</sup> nor OH<sup>•</sup> can be formed by the above pathways. Compared with basic solutions, acidic solutions are more efficient in the degradation of MO. A reason for this is the possible reaction of sodium ions (dissociated from MO or buffer components) with adsorbed OH<sup>•</sup> to form -ONa, which reduces the OH<sup>•</sup> amount [51]. Another explanation for this is that increased pH changes MO from quinoid to azo structure [49], which is harder to degrade. The

photocatalytic degradation efficiencies of MO at pH values of 4, 5 and 6 over V<sub>2</sub>O<sub>5</sub>/TiO<sub>2</sub> were 95.65, 66.43 and 56.32%, respectively.

**Effect of catalyst loading.** Figure 16 shows the effect of catalyst loading on MO dye degradation over the calcined [VOL<sup>1</sup>(DMF)]/TiO<sub>2</sub> using sunlight. The catalyst loadings were 5, 10, 15 and 20 mg L<sup>-1</sup>. The MO% removal upon increasing the amount of catalyst to 10 mg L<sup>-1</sup> over V<sub>2</sub>O<sub>5</sub>/TiO<sub>2</sub> sunlight and then decreasing it is shown in the figure. It should be indicated that the number of photocatalyst active sites and the penetration of radiation through the suspension is affected by the catalyst loading. As the catalyst loading increases, the MO% removal decreases because of the enhanced light reflectance by V<sub>2</sub>O<sub>5</sub>/TiO<sub>2</sub>. The number of active sites increases, but the infiltration of radiation decreases as a result of the shielding effect [52]. Thus, photocatalytic degradation rate, which is affected by both the penetration of irradiation light and the number of active sites, must pass through a maximum at optimum catalyst loading. In addition, the decreased adsorption density upon increasing the adsorbent amount results from the high number of unsaturated adsorption sites [53]. It should also be pointed out that the optimum catalyst loading value strongly depends on the type and initial concentration of the pollutant and the operating conditions of the photoreactor [54]. The optimal catalyst loading for V<sub>2</sub>O<sub>5</sub>/TiO<sub>2</sub> in this work was 10 mg L<sup>-1</sup> under sunlight. The

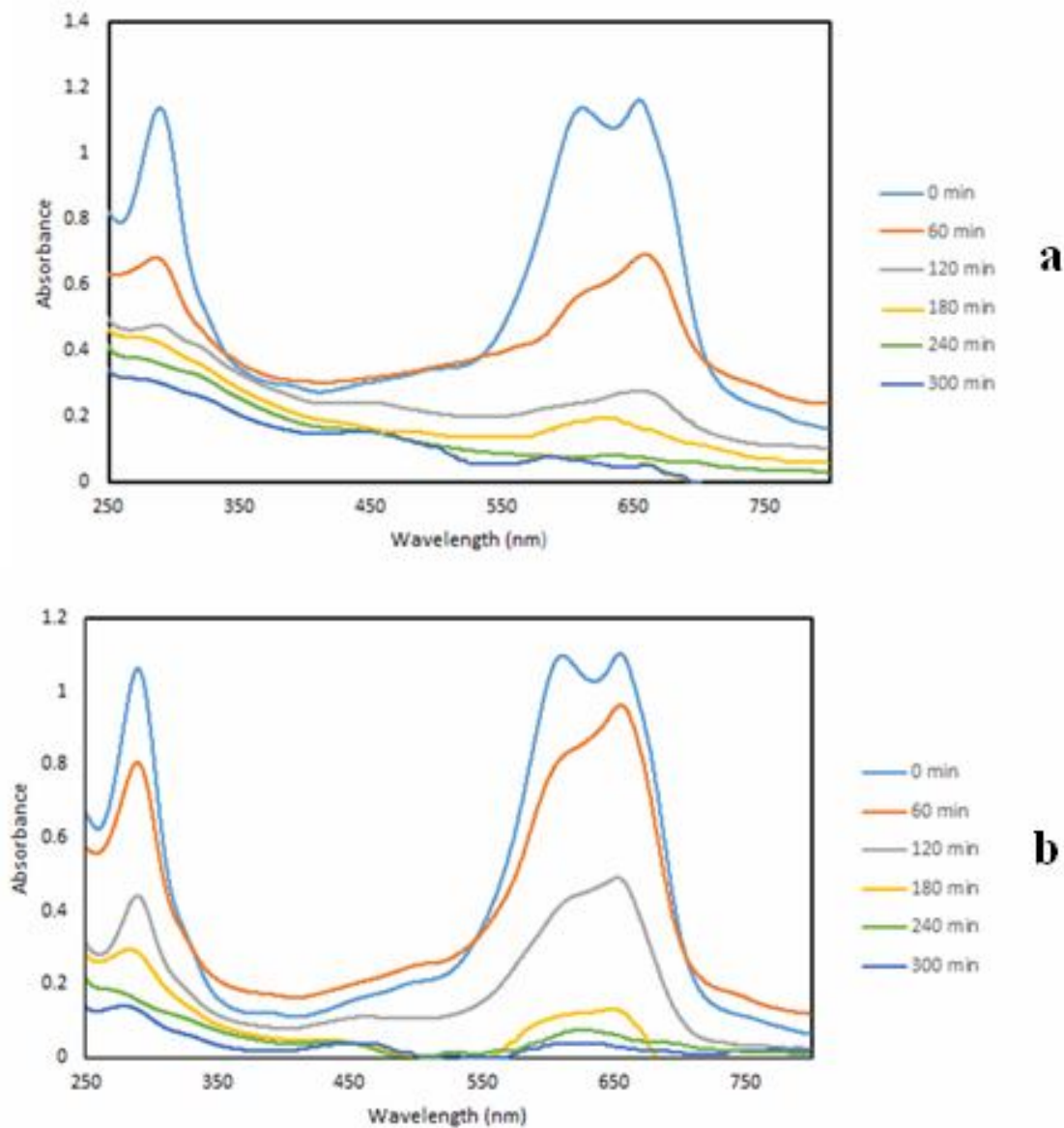


**Fig. 18.** (a) UV-Visible absorption spectra of aqueous solution of MB during degradation in the presence of calcined  $[\text{VOL}^1(\text{DMF})]/\text{TiO}_2$  and (b) UV-Vis absorption spectra of aqueous solution of MB during degradation in the presence of calcined  $[\text{VO}_2\text{L}^2]/\text{TiO}_2$  under sunlight at different times.

percent MO removals over  $\text{V}_2\text{O}_5/\text{TiO}_2$  under sunlight during 100 min irradiation time and  $\text{pH} = 4$  were 60.10, 71.81, 69.23 and 43.78% for 5, 10, 15 and 20  $\text{mg L}^{-1}$  of  $\text{V}_2\text{O}_5/\text{TiO}_2$ , respectively.

**Effect of time.** In order to investigate the effect of time on the photocatalytic degradation of MO under the optimized conditions of  $\text{pH} = 4$ , 10 mg of photocatalyst and

initial MO dye concentration of 5 ppm, the reaction was performed for up to 250 min. The results of this test are shown in Fig. 17. As it is known, the color of MO dye solution is the most intense in the first 60 min of degradation and over time, the sharp color decreases. The reason for this is the rapid decomposition of MO in the first 60 min by free radicals caused by the electron excitation of

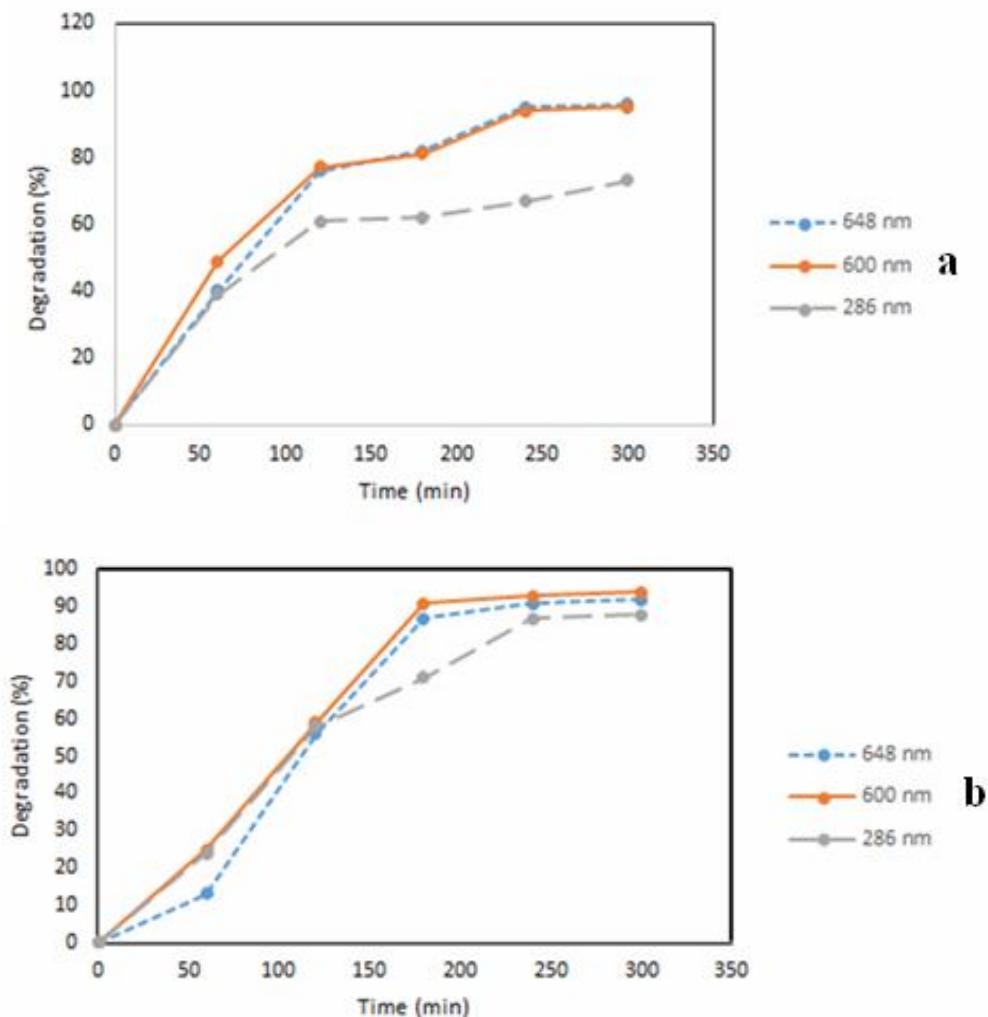


**Fig. 19.** (a) Degradation efficiency of aqueous solution of MB in the presence of calcined  $[\text{VOL}^1(\text{DMF})]/\text{TiO}_2$  and (b) UV-Vis absorption spectra of aqueous solution of MB during degradation in the presence of calcined  $[\text{VO}_2\text{L}^2]/\text{TiO}_2$  under sunlight.

modified titanium dioxide nanoparticles. Over time, due to the formation of intermediate organic compounds resulting from the decomposition of MO, some free radicals are produced to decompose these compounds and thus reduce the extent of methyl orange removal.

#### Qualitative Study of Photocatalytic Properties of Modified $\text{TiO}_2$ Samples under Sunlight

MB and MO degradations were also carried out in the presence of modified  $\text{TiO}_2$  samples under sunlight and monitored by UV-Vis spectroscopy. To prepare samples for

UV-Vis spectroscopy, 3 mL of the suspension were removed from the samples every 60 min and centrifuged to remove the nanoparticles.

#### Methylene blue degradation test under sunlight.

The photodegradation of MB was carried out under UV irradiation in the presence of calcined  $[\text{VOL}^1(\text{DMF})]/\text{TiO}_2$  (Fig. 18a) and  $[\text{VO}_2\text{L}^2]/\text{TiO}_2$  (Fig. 18b). The optical absorption intensity of MB in the solution, which contained  $\text{V}_2\text{O}_5/\text{TiO}_2$ , decreased with time. This clearly indicates that MB was degraded in 300 min. The UV spectrum shows several clear peaks at 648, 600 and

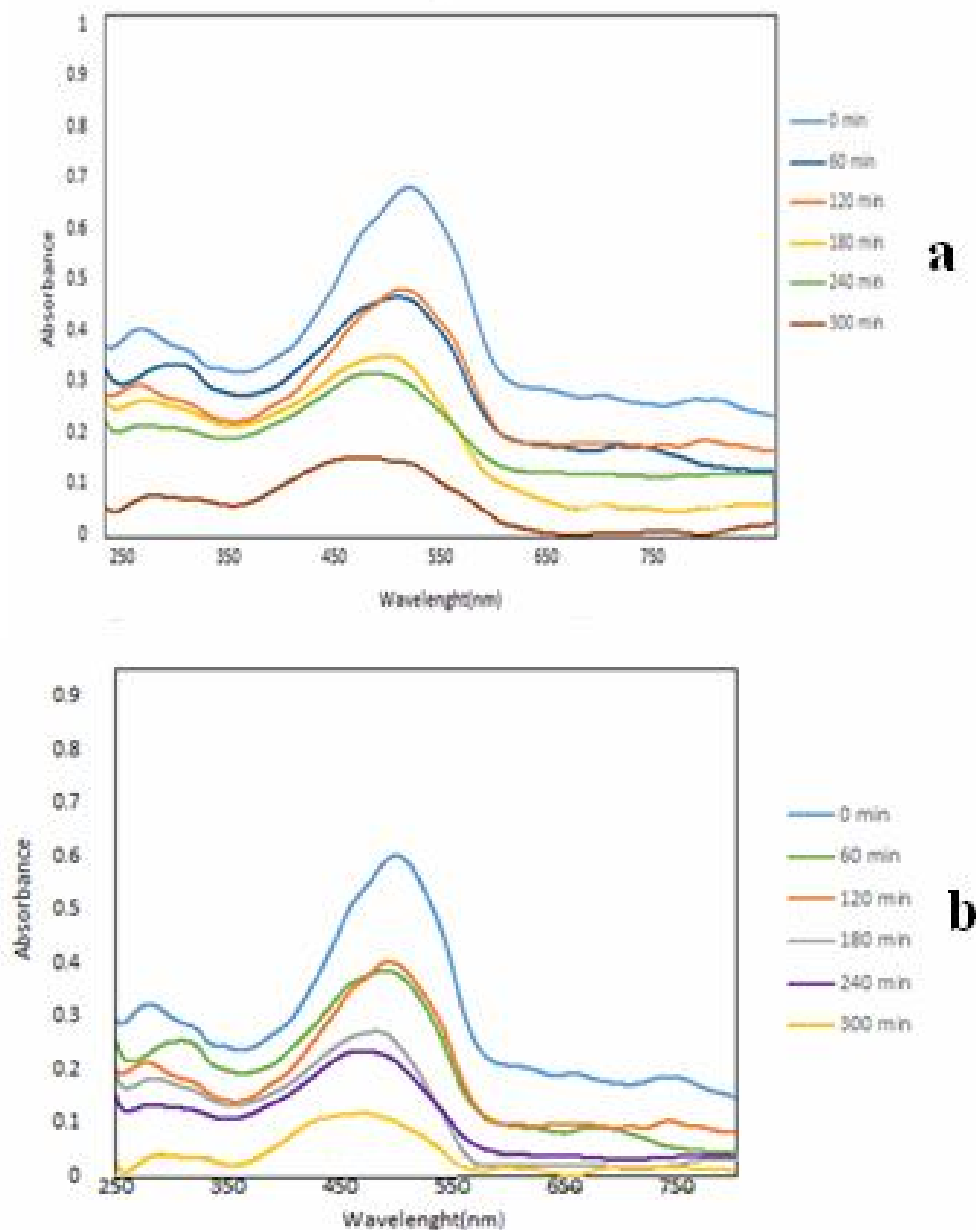


**Fig. 20.** (a) UV-Vis absorption spectra of aqueous solution of MO during degradation in the presence of calcined  $[VOL^1(DMF)]/TiO_2$  and (b) UV-Vis absorption spectra of aqueous solution of MB during degradation in the presence of calcined  $[VO_2L^2]/TiO_2$  under sunlight at different times.

286 nm. The degradation efficiency of MB can be calculated by this spectrum using the peak absorption at any time (Fig. 19). The degradation efficiency for MB by calcined  $[VOL^1(DMF)]/TiO_2$  at 648 nm was 99.32% in 300 min while that by calcined  $[VO_2L^2]/TiO_2$  was

92.56%). As observed, the photocatalytic degradation efficiency of MB over calcined  $[VOL^1(DMF)]/TiO_2$  was higher than that of calcined  $[VO_2L^2]/TiO_2$  under the same conditions.

**Methyl orange degradation test under sunlight.** MO

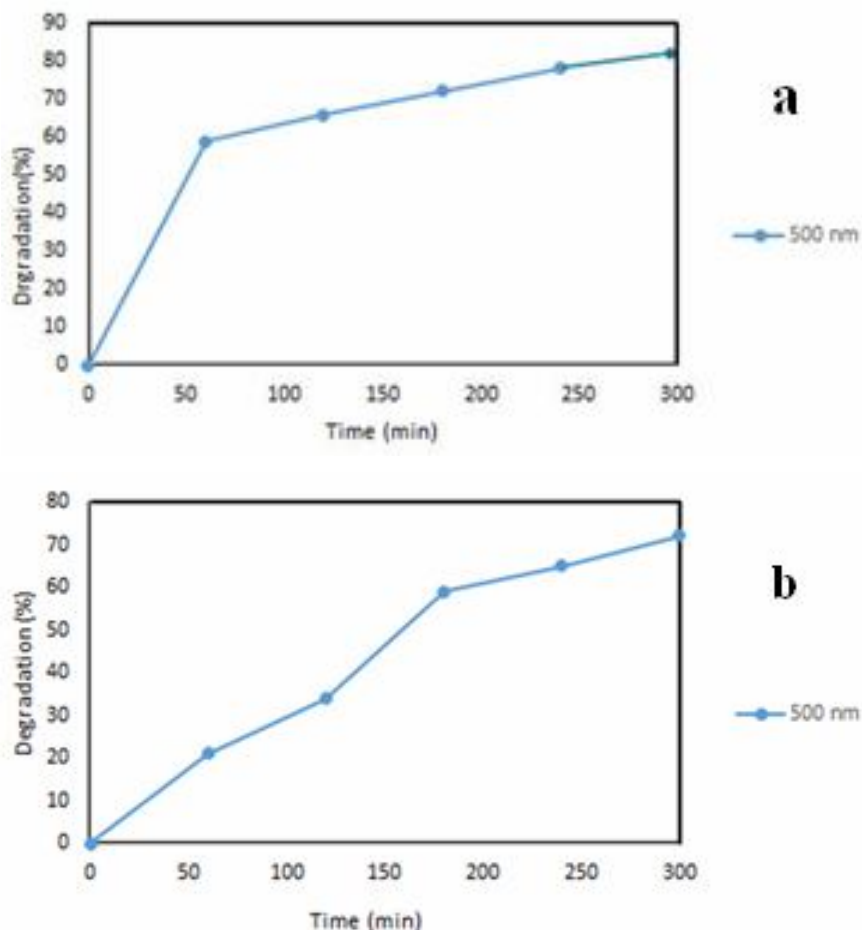


**Fig. 21.** (a) Degradation efficiency of aqueous solution of MO in the presence of calcined [VOL<sup>1</sup>(DMF)]/TiO<sub>2</sub> and (b) UV-Vis absorption spectra of aqueous solution of MB during degradation in the presence of calcined [VO<sub>2</sub>L<sup>2</sup>]/TiO<sub>2</sub> under sunlight.

photodegradation was performed under UV-Vis irradiation in the presence of calcined [VOL<sup>1</sup>(DMF)]/TiO<sub>2</sub> (Fig. 20a) and [VO<sub>2</sub>L<sup>2</sup>]/TiO<sub>2</sub> (Fig. 20b). The optical absorption intensity of MO in the solution, which contained V<sub>2</sub>O<sub>5</sub>/TiO<sub>2</sub>, decreased with time. This clearly indicates that MO was degraded in 300 min. The UV-Vis spectrum shows a certain peak at 500 nm. The degradation efficiency of MO degradation can be determined by this spectrum using the peak absorption at 500 nm at any time (Fig. 21). The degradation efficiencies of MO by calcined [VOL<sup>1</sup>(DMF)]/TiO<sub>2</sub> and [VO<sub>2</sub>L<sup>2</sup>]/TiO<sub>2</sub> were 80.14% and 71.24%, respectively, in 300 min. The photocatalytic

degradation efficiency of MO over calcined [VOL<sup>1</sup>(DMF)]/TiO<sub>2</sub> was higher than that of calcined [VO<sub>2</sub>L<sup>2</sup>]/TiO<sub>2</sub> under the same conditions.

## CONCLUSIONS

In this work, two tridentate Schiff base ligands and their oxidovanadium Schiff base complexes were synthesized and characterized. The photocatalytic activity of the new nanoparticles was evaluated in the decomposition of methylene blue (MB) and methyl orange (MO) dyes in aqueous media under visible light and sunlight. In order to

provide a well-shaped nanostructure for photocatalytic reactions, the synthesized complexes [VOL<sup>1</sup> (DMF)] and [VO<sub>2</sub>L<sup>2</sup>] were applied as a solid supports for TiO<sub>2</sub> nano metal oxide. Different analytical methods such as FT-IR spectroscopy, scanning electron microscopy and X-ray diffraction analysis were used to characterize these photocatalysts. The band gap energies of the doped TiO<sub>2</sub> samples were remarkably narrower than those of pure TiO<sub>2</sub>. Loading titania with vanadium metal significantly affected the catalytic activity during dye degradation reactions, according to the results obtained.

## SUPPORTING INFORMATION

Crystallographic data deposited at the Cambridge Crystallographic Data Centre under CCDC-1900825 for VO<sub>2</sub>L<sup>2</sup> contain the supplementary crystallographic data excluding structure factors. This data can be obtained free of charge *via* [www.ccdc.cam.ac.uk/conts/retrieving.html](http://www.ccdc.cam.ac.uk/conts/retrieving.html) (or from the Cambridge Crystallographic Data Centre, 12, Union Road, Cambridge CB2 1EZ, UK; fax: (+44) 1223-336-033; or [deposit@ccdc.cam.ac.uk](mailto:deposit@ccdc.cam.ac.uk)).

## ACKNOWLEDGMENTS

This work was financially supported by Isfahan University of Technology. The authors gratefully acknowledge Iran National Science Foundation for its financial support.

## REFERENCES

- [1] G. Mohammadnezhad, R. Debel, W. Plass, *J. Mol. Catal. A Chem.* 410 (2015) 160.
- [2] J.Q. Xie, C.H. Li, J.X. Dong, W. Qu, L. Pan, M.L. Peng, M.A. Xie, X. Tao, C.M. Yu, Y. Zhu, P.H. Zhang, C.G. Tang, Q.G. Li, *Thermochim. Acta* 598 (2014) 7.
- [3] M. Ikram, S. Rehman, A. Khan, R.J. Baker, T.S. Hofer, F. Subhan, M. Qayum, Faridoon, C. Schulzke, *Inorg. Chim. Acta* 428 (2015) 117.
- [4] O.A.M. Ali, S.M. El-Medani, D.A. Ahmed, D.A. Nassar, *J. Mol. Struct.* 1074 (2014) 713.
- [5] J.-P. Cao, L.-L. Zhou, L.-Z. Fu, J.-X. Zhao, H.-X. Lu, S.-Z. Zhan, *Catal. Commun.* 57 (2014) 1.
- [6] G. Mohammadnezhad, M. Böhme, D. Geibig, A. Burkhardt, H. Görls, W. Plass, *Dalton Trans.* 42 (2013) 11812.
- [7] P.A. Nikolaos, P. Xekoukoulotakis, D. Mantzavinos, *Water Res.* 40 (2006) 1276.
- [8] M. Muruganandham, M. Swaminathan, *Sol. Energ. Mat. Sol. C* 81 (2004) 439.
- [9] M. Kositzi, A. Antoniadis, I. Poullos, I. Kiridis, S. Malato, *Sol. Energ.* 77 (2004) 591.
- [10] T. Velegraki, I. Poullos, M. Charalabaki, N. Kalogerakis, P. Samaras, D. Mantzavinos, *Appl. Catal. B: Environ.* 62 (2006) 159.
- [11] T. Sauer, G. Cesconeto Neto, H.J. Jose, R.F.P.M. Moreira, *J. Photochem. Photobiol. A: Chem.* 149 (2002) 147.
- [12] C.M. So, M.Y. Cheng, J.C. Yu, P.K. Wong, *Chemosphere* 46 (2002) 905.
- [13] S. Malato, P. Fernandez-Ibanez, M.I. Maldonado, J. Blanco, W. Gernjak, *Catal. Today* 147 (2009) 1.
- [14] J.L. Gole, J.D. Stout, C. Burda, *J. Phys. Chem. B* 108 (2004) 1230.
- [15] K.T. Ranjit, I. Willner, S.H. Bossmann, A.M. Braun, *J. Catal.* 204 (2001) 305.
- [16] J.W. Shi, J.T. Zheng, Y. Hu, Y.C. Zhao, *J. Mater. Chem. Phys.* 106 (2007) 247.
- [17] E. Kowalska, H. Remita, C. Colbeau-Justin, J. Hupka, J. Belloni, *J. Phys. Chem. C* 112 (2008) 1124.
- [18] X. Quan, Q. Zhao, H. Tan, X. Sang, *J. Mater. Chem. Phys.* 114 (2009) 90.
- [19] W. Choi, A. Termin, M.R. Hoffmann, *J. Phys. Chem.* 98 (1994) 13669.
- [20] X.X. Yang, C. Cao, K. Hohn, L. Erickson, *J. Catal.* 252 (2007) 296.
- [21] S.T. Martin, C.L. Morrison, M.R. Hoffmann, *J. Phys. Chem.* 98 (1994) 13695.
- [22] Z.M. Tian, S.L. Yuan, S.Y. Yin, S.Q. Zhang, H.Y. Xie, *J. Magn. Magn. Mater.* 320 (2008) L5.
- [23] S. Liu, T. Xie, Z. Chen, J. Wu, *J. Appl. Surf. Sci.* 255 (2009) 8587.
- [24] A.H. Kianfar, M. Dostani, *J. Mater. Sci.: Mater. El.* 28 (2017) 7353.
- [25] M. Dostani, A.H. Kianfar, M.M. Momeni, *J. Mater. Sci.: Mater. El.* 28 (2017) 633.

- [26] A.H. Kianfar, H. Farrokhpour, P. Dehghani, *Spectrochim. Acta. A: Mol. Biomol. Spectrosc.* 150 (2015) 220.
- [27] COLLECT, Data Collection Software; Nonius B.V., Netherlands, 1998
- [28] Z. Otwinowski, W. Minor, Processing of X-Ray Diffraction Data Collected in Oscillation Mode“, in *Methods in Enzymology*, Vol. 276, Macromolecular Crystallography, Part A, Edited by C.W. Carter, R.M. Sweet, Academic Press, San Diego, USA, 1997, pp. 307-326.
- [29] SADABS 2016/2: L. Krause, R. Herbst-Irmer, G.M. Sheldrick, D. Stalke, *J. Appl. Cryst.* 48 (2015) 3.
- [30] G.M. Sheldrick, *Acta Cryst. C* 71 (2015) 3.
- [31] I. Sheikhshoae, Y. Ebrahimipour, N. Lotfi, *Inorg. Chim. Acta* 442 (2016) 151.
- [32] A.H. Kianfar, L. Keramat, M. Dostani, M. Shamsipur, M. Roushani, F. Nikpour, *Spectrochim. Acta A* 77 (2010) 424.
- [33] A.A.A. Emara, *Spectrochim. Acta A* 77 (2010) 117.
- [34] G. Mul, A. Zwijnenburg, B. van der Linden, M. Makkee, J.A. Moulijn, *J. Catal.* 201 (2001) 128.
- [35] P. Du, A. Bueno Lopez, M. Verbaas, A.R. Almeida, G. Mul, *J. Catal.* 260 (2008) 75.
- [36] T. Lopez, J.A. Moreno, R. Gomez, X. Bokhimi, J.A. Wang, H. Yee Madeira, G. Pecchi, P. Reyes, *J. Mater. Chem.* 12 (2002) 1.
- [37] A.H. Kianfar, V. Sobhani, M. Dostani, M. Shamsipur, M. Roushani, *Inorg. Chim. Acta* 355 (2011) 108.
- [38] A.H. Kianfar, M. Dostani, *Spectrochim. Acta* 82 (2011) 69.
- [39] J. Yan, G. Wu, N. Guan, L. Li, Z. Li, X. Cao, *Phys. Chem. Chem. Phys.* 15 (2013) 10978.
- [40] M.A. Behnajady, H. Eskandarloo, N. Modirshahla, M. Shokri, *Desalination* 278 (2011) 10.
- [41] J.G. Yu, Y.R. Su, B. Cheng, *Adv. Funct. Mater.* 17 (2007) 1984.
- [42] M.M. Momeni, Y. Ghayeb, M. Davarzadeh, *J. Mater. Sci.: Mater. Electron.* 26 (2015) 1560.
- [43] A.K.L. Sajjad, S. Shamaila, B. Tian, F. Chen, J. Zhang, *Appl. Catal.* 91 (2009) 397.
- [44] A.K.L. Sajjad, S. Shamaila, B. Tian, F. Chen, J. Zhang, *J. Hazard Mater.* 177 (2010) 781.
- [45] I.K. Konstantinou, T.A. Albanis, *Appl. Catal.* 42 (2003) 319.
- [46] G. Pecchi, P. Reyes, P. Sanhueza, *Chemosphere* 43 (2001) 141.
- [47] D. Wang, J. Zhang, Q. Luo, X. Li, Y. Duan, J. An, *J. Hazard. Mater.* 169 (2009) 546.
- [48] P. Salvador, *J. Phys. Chem. C* 111 (2007) 17038.
- [49] N. Barka, A. Assabbane, A. Nounah, J. Dussaud, Y.A. Ichou, *Phys. Chem. News.* 41 (2008) 85.
- [50] L. Gan, X. Wang, Zh. Hao, *Tongji Daxue Xuebao Ziran Kexunban.* 33 (2005) 1078.
- [51] J. Wang, B. Xin, H. Yu, *Gaodeng Xuexiao Huaxue Xuebao.* 24 (2003) 1093.
- [52] M.S.T. Goncalves, A.M.F. Oliveira Compos, E.M.M.S. Pinto, P.M.S. Plasencia, M.J.R.P. Queiroz, *Chemosphere* 39 (1999) 781.
- [53] M.R. Salim, F. Othman, M.D. Imtiaz Ali, J. Patterson, T. Hardy, *Water Sci. Technol.* 46 (2002) 339.
- [54] P.R. Gogate, A.B. Pandit, *Adv. Environ. Res.* 8 (2004) 501.